

Visualizing the Hidden Features of Galaxy Morphology with Machine Learning

Jia-Ming Dai,^{1,2} [★] Jizhou Tong¹

¹ National Space Science Center, Chinese Academy of Sciences, Beijing 100190, China

² University of Chinese Academy of Sciences, Beijing 100049, China

Accepted XXX. Received YYY; in original form ZZZ

ABSTRACT

We train three convolutional neural networks (CNNs) to classify galaxies with Galaxy Zoo 2 dataset and extract the activations from the last fully connected layer or the last average pooling layer of CNNs to study the high-dimensional abstract feature representations of galaxy images. We apply t-Distributed Stochastic Neighbour Embedding (t-SNE), a popular dimensionality reduction technique, to visualize the high-dimensional galaxy feature representations in two-dimensional scatter plots. From the visualization, we try to understand the galaxy images data itself and obtain some highly valuable insights. For instance, the learned galaxy feature representations from networks indicate that the galaxies belonging to the same class tend to group together, i.e. same morphological galaxies are clustered; The cluster of completely round smooth galaxy and the cluster of in-between smooth galaxy (between completely round and cigar-shaped) are moved closer, compared to other clusters; The cluster of cigar-shaped smooth galaxy and the cluster of edge-on galaxy are intertwined surprisingly; A galaxy mislabelled as spiral galaxy in the original dataset falls in the cluster of completely round smooth galaxy, and manual inspection also identifies out the outlier as a completely round smooth galaxy. These findings will facilitate the study of galaxy morphology.

Key words: methods: data analysis-techniques: image processing-galaxies: general.

1 INTRODUCTION

Deep learning has been increasingly applied to galaxy morphology classification and achieved a series of success. For example, Dieleman et al. (2015) first used CNNs to galaxy morphology classification which exploits galaxy images translation and rotation invariance on Galaxy Zoo 2 dataset. Gravet et al. (2015) used the Dieleman model to classify high redshift galaxies in the 5 Cosmic Assembly Near-infrared Deep Extragalactic Legacy Survey (CANDELS). Kim & Brunner (2016) used CNNs to resolve star-galaxy classification. Aniyán & Thorat (2017) used CNNs to classify radio galaxies into FRI, FRII and Bent-tailed radio galaxies. Sánchez et al. (2017) used CNNs to improve galaxy morphologies for Sloan Digital Sky Survey (SDSS). These works focus on the classification tasks however we argue that these works can go further by digging into the networks to analyse what features can be learned and how the learned features can help in a better understanding of the data itself. It is well known that the reason for CNNs

to have been used so popularly and successfully in galaxy morphology classification lies in that CNNs can be fed with raw data directly and can automatically learn the feature representations needed for classification task (Bengio et al. 2013; LeCun et al. 2015). These learned feature representations are nonlinear mappings of the original image pixel values, although they are still high-dimensional, they can be used not only for classification, but also for other purposes, such as dimensionality reduction and visualization.

Visualization of high-dimensional data is one of the methods of data analysis and can discover a lot of highly valuable feedbacks. In the last few decades a series of dimensionality reduction techniques have been proposed to visualize high-dimensional data due to the large high dimensional data in real world. Dimensionality reduction techniques include linear techniques, like Principal Components Analysis (PCA) (Hotelling 1933) and classical scaling (Torgerson 1952), and nonlinear techniques (Van Der Maaten 2007; Van Der Maaten et al. 2009), like Isomap (Tenenbaum et al. 2000), Locally linear Embedding (LLE) (Roweis & Saul 2000), Laplacian Eigenmaps (Belkin & Niyogi 2002), Auto-encoder (Hinton & Salakhutdinov 2006) and t-Distributed

[★] E-mail: daijiamingdl@gmail.com

Stochastic Neighbor Embedding (t-SNE) (Maaten & Hinton 2008; Van Der Maaten 2014). t-SNE is intensively applied to visualize high-dimensional data in machine learning due to its capability of preserving the local structure of the data and revealing global structure. Maaten & Hinton (2008) proposed t-SNE method and demonstrated its good performance with other dimensionality reduction techniques on a wide variety of datasets. Van Der Maaten (2014) trained CNNs to extract image feature representation, used t-SNE techniques to visualize high-dimensional data by scatter plots on MNIST (LeCun 1998) and SVHN (Netzer et al. 2011) datasets, and obtained some valuable insights and qualitative analysis. Recently, Rauber et al. (2017) systematically trained multilayer perceptrons (MLPs) and CNNs to extract activations from the last fully connected layer in three traditional image classification benchmark datasets (MNIST, SVHN and CIFAR-10), then used t-SNE techniques to visualize the learned presentations in two-dimensional scatter plots. Some highly valuable feedbacks were discovered.

These work inspires the study of the feature representations of galaxy morphology automatically learned from networks. We look deeply into the networks searching for the physical meanings of the high-dimensional abstract feature representations and show how these feature representations help to understand the galaxy images data itself. In this paper we train three CNNs to classify galaxies into five classes. We use activations from the last fully connected layer or the last average pooling layer of CNNs to make high-dimensional galaxy morphological feature representations and use t-SNE techniques to visualize the high-dimensional galaxy morphological feature representations in two-dimensional scatter plots. This is the first time to apply in galaxy morphology.

The outline of the paper is as follows. In Section 2, we introduce our three CNNs architectures, dataset selection, image preprocessing, training protocol, classification results and activations extraction. In Section 3, we outline t-SNE techniques and present the visualization of the learned feature representations in details. Our conclusions and suggestions for future work are presented in Section 4.

2 CLASSIFICATION FRAMEWORK

Deep learning models are composed of multiple nonlinear layers to learn data representation automatically for classification, detection and segmentation tasks. Among them, deep convolutional neural networks (CNNs) have become the dominant approach in image classification task (LeCun et al. 2015). Since 2012, when Krizhevsky et al. (2012) used a CNN to win the first place of the ImageNet Large Scale Visual Recognition Challenge (ILSVRC), CNNs have achieved a series of breakthroughs in image classification. Now, CNNs have been evolved into many versions, such as AlexNet (Krizhevsky et al. 2012), VGG (Simonyan & Zisserman 2014), Inception (Szegedy et al. 2015; Ioffe & Szegedy 2015; Szegedy et al. 2016, 2017), ResNets (He et al. 2016b,a), DenseNet (Huang et al. 2016) and so on. Full details are available in above literatures and Goodfellow et al. (2016).

In this section, we first describe dataset selection, data processing, three CNNs architectures and training tips. Next, the classification results are summarized. At last, we

extract the representation learned from networks as galaxy morphological features.

2.1 Dataset

The galaxy images in this study are drawn from Galaxy Zoo-the Galaxy Challenge¹ from Galaxy Zoo 2 (GZ2). In order to select clean samples, we use the rules of selecting clean samples of GZ2 data release (Willett et al. 2013). For example, to select the spiral, cuts are the combination of $f_{features/disk} \geq 0.430$, $f_{edge-on,no} \geq 0.715$ and $f_{spiral,yes} \geq 0.619$. By this means, we classify galaxies into 5 classes, i.e. completely round smooth galaxy, in-between smooth galaxy (between completely round and cigar-shaped), cigar-shaped smooth galaxy, edge-on galaxy and spiral galaxy, which are referred to as 0, 1, 2, 3, 4, respectively. We loosened the thresholds of smooth galaxy from 0.8 to 0.5 and all others are derived from Willett et al. (2013), where full details of this are available. Table 1 shows the clean samples selection criterion for every class. Dataset reduced to 28790 images after filtering. Each image is of $424 \times 424 \times 3$ pixels in size. We split them into training set and testing set at a ratio of 9:1, 25911 images are used to train models and the remaining 2879 images to evaluate our models.

2.2 Preprocessing

It can be seen that images are composed of large fields of view with the galaxy of interest in the center. So first step, galaxy images are cropped from center to a range scale $S = [170, 240]$ in training set. Almost main information is contained in the center images and many noises like other secondary objects are eliminated. It reduces the dimension of image and it is also a form of data augmentation for training set. Then, images are resized to $80 \times 80 \times 3$ pixels. A random crop is performed to $64 \times 64 \times 3$ pixels. Next, images are randomly rotated with $0^\circ, 90^\circ, 180^\circ, 270^\circ$ due to rotation invariant of galaxy images and randomly horizontally flipped. Brightness, contrast, saturation and hue adjustment are applied to images. These steps are data augmentation to avoid overfitting. The last step was image whitening. This are the whole preprocessing pipeline in training. After those steps, images ($64 \times 64 \times 3$ pixels) will be used as input of networks in training.

At testing time, preprocessing procedure only includes center cropping (test scale $Q = \{180, 200, 220, 240\}$), resizing to $80 \times 80 \times 3$ pixels, center cropping again, and image whitening. Images ($64 \times 64 \times 3$ pixels) will be used as input of networks in testing.

2.3 CNNs architectures

To extract feature representations from the galaxy images, we train three CNNs, as Table 2 shows:

(i) CNN 1: CNN 1 is a 7-layers CNN, including 4 convolutional layers and 3 fully connected layers. It is a slightly modified Dieleman model (Dieleman et al. 2015).

¹ <https://www.kaggle.com/c/galaxy-zoo-the-galaxy-challenge>

Table 1. Clean samples selection in GZ2. The clean galaxy images are selected from GZ2 data release (Willett et al. 2013), in which thresholds determine well-sampled galaxies. Thresholds depend on the number of votes for a classification task considered to be sufficient. As an example, to select the spiral, cuts are the combination of $f_{features/disk} \geq 0.430$, $f_{edge-on,no} \geq 0.715$, $f_{spiral,yes} \geq 0.619$.

Class	Clean sample	Tasks	Selection	N_{sample}
0	Completely round smooth	T01	$f_{smooth} \geq 0.469$	8434
		T07	$f_{completely\ round} \geq 0.50$	
1	In between smooth	T01	$f_{smooth} \geq 0.469$	8069
		T07	$f_{in\ between} \geq 0.50$	
2	Cigar-shaped smooth	T01	$f_{smooth} \geq 0.469$	578
		T07	$f_{cigar-shaped} \geq 0.50$	
3	Edge-on	T01	$f_{features/disk} \geq 0.430$	3903
		T02	$f_{edge-on,yes} \geq 0.602$	
4	Spiral	T01	$f_{features/disk} \geq 0.430$	7806
		T02	$f_{edge-on,no} \geq 0.715$	
		T04	$f_{spiral,yes} \geq 0.619$	

Table 2. Our three CNNs architectures. First column represents “type” for CNN 1 and CNN 2, fifth column represents “layer name” for CNN 3.

Type	CNN 1	CNN 2	CNN 3	Layer name
convolutional	$6 \times 6, 32$	$3 \times 3, 64$	$6 \times 6, 64$	conv 1
convolutional	-	$3 \times 3, 64$	-	-
pooling	2×2 , stride 2	2×2 , stride 2	2×2 , stride 2	max-pooling
convolutional	$5 \times 5, 64$	$3 \times 3, 128$	$\begin{bmatrix} 1 \times 1, 128 \\ 3 \times 3, 128 \end{bmatrix} \times 2$	conv 2
convolutional	-	$3 \times 3, 128$		
pooling	2×2 , stride 2	2×2 , stride 2	$\begin{bmatrix} 1 \times 1, 512 \end{bmatrix}$	
convolutional	$3 \times 3, 128$	$3 \times 3, 256$	$\begin{bmatrix} 1 \times 1, 256 \\ 3 \times 3, 256 \end{bmatrix} \times 2$	conv 3
convolutional	$3 \times 3, 128$	$3 \times 3, 256$		
convolutional	-	$3 \times 3, 256$	$\begin{bmatrix} 1 \times 1, 1024 \end{bmatrix}$	
pooling	2×2 , stride 2	2×2 , stride 2	$\begin{bmatrix} 1 \times 1, 512 \\ 3 \times 3, 512 \end{bmatrix} \times 2$	conv 4
convolutional	-	$3 \times 3, 512$	$\begin{bmatrix} 1 \times 1, 2048 \end{bmatrix}$	
convolutional	-	$3 \times 3, 512$	$\begin{bmatrix} 1 \times 1, 1024 \\ 3 \times 3, 1024 \end{bmatrix} \times 2$	conv 5
pooling	-	2×2 , stride 2		
convolutional	-	$3 \times 3, 512$	$\begin{bmatrix} 1 \times 1, 4096 \end{bmatrix}$	
convolutional	-	$3 \times 3, 512$		
convolutional	-	$3 \times 3, 512$		
pooling	-	2×2 , stride 2	4×4	avg-pooling
fully-connected	2048	4096		
fully-connected	2048	4096		
fully-connected	5	5	5	softmax

(ii) CNN 2: CNN 2 has 16 layers totally, 13 convolutional layers and 3 fully connected layers. It is a slightly modified VGG-16 (Simonyan & Zisserman 2014).

(iii) CNN 3: CNN 3 is a modified ResNets (He et al. 2016b,a), 26 layers totally, where we decrease the depth and widen the channel. It has 4 convolutional groups: conv2, conv3, conv4 and conv5, respectively. We add dropout after 3×3 convolution of every residual unit, to prevent coadaptation and overfitting. Downsampling is performed by the last layers in groups conv2, conv3 and conv4 with a stride of 2.

2.4 Training

The activation function of all convolutional layers and fully connected layers (except output layer) is Rectified Linear Units (ReLU) (Nair & Hinton 2010). The networks are trained to minimize cross entropy loss. We use a batch size of 128. The initial learning rate is set to 0.1, then decreased by a factor of 10 at 30k and 60k iterations.

For CNN 1, we use GradientDescentOptimizer. We stop training after 72k iterations. Weights are initialized by sam-

pling from zero-mean normal distributions (standard deviation 0.01 for convolutional layers and softmax layer, standard deviation 0.001 for fully connected layers). Biases are initialized to small positive values (0.1 for convolutional layers and softmax layer, 0.01 for fully connected layers). Dropout probability value is 0.5 (Srivastava et al. 2014).

For CNN 2, we use GradientDescentOptimizer. We stop training after 42k iterations. All weights are initialized by Xavier initializer (Glorot & Bengio 2010). Biases are initialized to 0 for convolutional layers (0.1 for fully connected layers and softmax layer). The weight loss values of the two fully connected layers are 0.0005. Dropout probability value is 0.5.

For CNN 3, we use MomentumOptimizer with Nesterov momentum of 0.9, the weight decay is 0.0001, dropout probability value is 0.8. We adopt batch normalization (BN) (Ioffe & Szegedy 2015) before activation and convolution, following He et al. (2016a). The weights are initialized as in He et al. (2015). We stop training after 72k iterations.

Our implementation is based on Python, Pandas, scikit-

Table 3. Test accuracy of different methods. Our results are based on the maximum values of 10-times runs of each test scale.

Model	Overall Accuracy(%)
CNN 1	94.6528
CNN 2	93.6458
CNN 3	95.2083

learn (Pedregosa et al. 2012), scikit-image (Van et al. 2014) and TensorFlow (Abadi et al. 2016).

2.5 Classification results

Table 3 summaries the results of test accuracy of different methods. Our results are based on the maximum values of 10-times runs of each testing scale. It is obvious all three models of ours achieve excellent performance.

2.6 Activations

A subset of 1000 images is extracted from training set, each class contains 200 images, which is hence called training-1000. And a random subset of 1000 images is also extracted from testing set, each class contains 200 images (the cigar-shaped is not enough and only has 58 images, in addition 142 image are extracted from training set), hence it is called testing-1000. For CNN 1, we use the activations in the last fully connected layer as 2,048-dimensional feature representations. For CNN 2, we use the activations in the last fully connected layer as 4,096-dimensional feature representations. For CNN 3, we use the activations in the average pooling layers as 4,096-dimensional feature representations, respectively.

3 VISUALIZING THE LEARNED FEATURE REPRESENTATIONS

In this section, we briefly introduce t-Distributed Stochastic Neighbor Embedding (t-SNE) technique, and then use it to visualize the high-dimensional galaxy morphological feature representations learned from CNNs.

3.1 t-SNE

t-Distributed Stochastic Neighbor Embedding (t-SNE) is a popular dimensionality reduction algorithm presented in Maaten & Hinton (2008); Van Der Maaten (2014). It is a nonlinear dimensionality reduction method which is especially suitable for the visualization of high-dimensional data in a space of two or three dimension, this is so-called a scatter plot. And it is an extremely broadly applicable technique in machine learning due to its capability of preserving the local structure of the data and revealing the global structure.

A dataset X includes N observations $X = \{x_1, x_2, \dots, x_N\}$, where are D -dimensional real vector. The goal of t-SNE is to compute a projection $Y = \{y_1, y_2, \dots, y_N\}$ where the neighborhoods from D are preserved, generally, $y_i \in \mathbb{R}^d$ corresponds to $x_i \in \mathbb{R}^D$. Typically, $d = 2$ and $D \gg d$.

Firstly, compute conditional probability $p_{j|i}$ that are

proportional to the similarity of datapoint x_i and datapoint x_j . $p_{j|i}$ is high when x_i is near to x_j and $p_{j|i}$ is defined as

$$p_{j|i} = \frac{\exp(-\|x_i - x_j\|^2/2\sigma_i^2)}{\sum_{k \neq i} \exp(-\|x_i - x_k\|^2/2\sigma_i^2)}. \quad (1)$$

where σ_i is the variance of the Gaussian that is centered on datapoint x_i .

Then, define the joint probabilities p_{ij} in the high-dimensional space to be the symmetrized conditional probabilities

$$p_{ij} = \frac{p_{j|i} + p_{i|j}}{2N}. \quad (2)$$

Next, in the low-dimensional space, define the joint probabilities q_{ij} which uses a Student t-distribution with one degree of freedom (which is the same as a Cauchy distribution) as the heavy-tailed distribution

$$q_{ij} = \frac{(1 + \|y_i - y_j\|^2)^{-1}}{\sum_{k \neq i} (1 + \|y_k - y_i\|^2)^{-1}}. \quad (3)$$

t-SNE aims at minimizing the following cost function C . And the locations of the points y_i in the map are determined by minimizing the Kullback-Leibler divergence of the distribution Q from the distribution P , that is

$$C = KL(P|Q) = \sum_i \sum_j p_{ij} \log \frac{p_{ij}}{q_{ij}}. \quad (4)$$

The gradient of the Kullback-Leibler divergence between P and the Student-t based joint probability distribution Q is given by

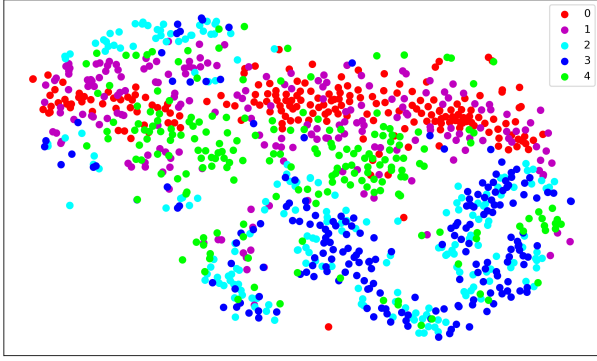
$$\frac{\delta C}{\delta y_i} = 4 \sum_j (p_{ij} - q_{ij})(y_i - y_j)(1 + \|y_i - y_j\|^2)^{-1}. \quad (5)$$

For further more details, we refer to Maaten & Hinton (2008); Van Der Maaten (2014).

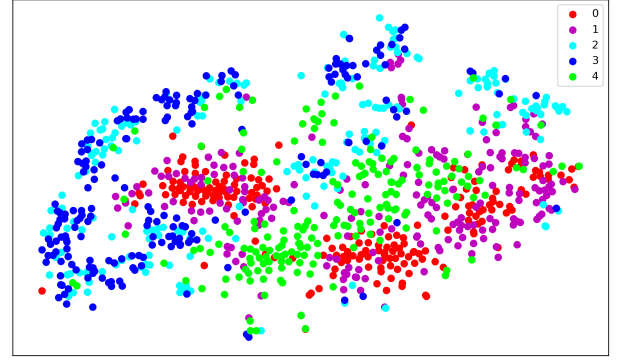
3.2 Visualizing the representations

Figure 1 presents visualizations of raw samples. We color all points by their classes, and each point is a galaxy image. Figure 1a shows the classes of galaxy have a poor separation and are quite tangled on training-1000 subset. Similar result on testing-1000 subset is shown in Figure 1b as well. It happens due to the absence of the use of supervised (labels) information before training. And both of the Figure 1a and Figure 1b indicate our dataset is complex and challenging.

Figure 2 shows visualizations of activations of the last fully connected layer of CNN 1. We color all points by their classes, and mark misclassification by triangle glyphs. It can be seen that the visual separation among galaxy classes both on training-1000 subset and testing-1000 subset is improved significantly after training. As LeCun et al. (2015) said, higher layers of representation amplify aspects of the input that are important for classification and discrimination. Figure 2a and Figure 2b show that the last fully connected layer of CNN 1 has learned to transform the raw data into a nice representation and the classes are much more separated.

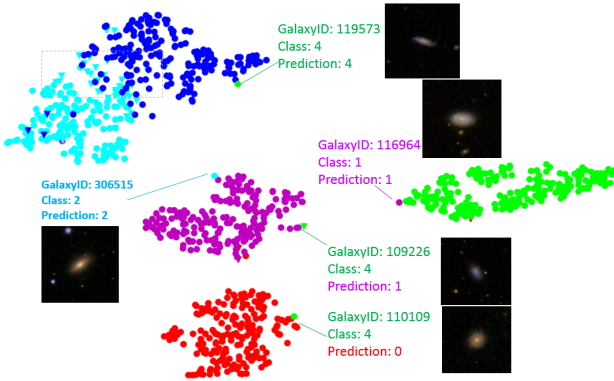


(a) Map of raw samples on the training-1000 subset.

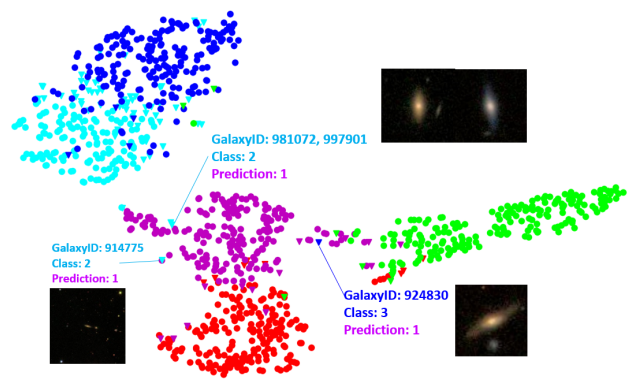


(b) Map of raw samples on the testing-1000 subset.

Figure 1. Visualizations of raw samples. We color all points by their classes, and each point is a galaxy image.



(a) Map of the last fully connected layer of CNN 1 on the training-1000 subset. (Accuracy: 94.9%)



(b) Map of the last fully connected layer of CNN 1 on the testing-1000 subset. (Accuracy: 90.4%)

Figure 2. Visualizations of activations of the last fully connected layer of CNN 1. We color all points by their classes, and mark misclassification by triangle glyphs. Each point is a galaxy image.

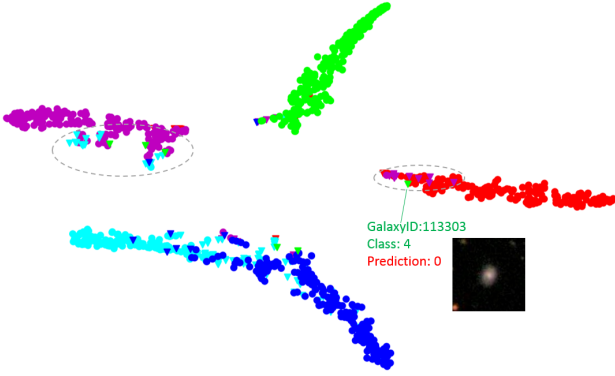
From the visualizations, the images of each galaxy morphological class are presence of clusters, i.e. each class of galaxy images is grouped, the images with same morphological class are moved closer together. It can be explained that the images of same galaxy morphological class have similar underlying structure, so they tend to be grouped in scatter plots. From Figure 2b, we also can find the completely round and the in-between are closer, compared to other galaxy clusters. It is caused that the completely round and the in-between belong to a broad cluster, namely, smooth galaxy.

Then, inspecting the outliers is interesting. Consider the lime point placed in the bottom of blue cluster in Figure 2a, which belongs to the spiral and is predicted to the spiral as well, but it has the similar structure with the edge-on. When inspected, the outlier sample (the spiral: GalaxyID 119573) looks very similar to the edge-on class. Many other outliers (the cigar-shaped: GalaxyID 306515 and the in-between: GalaxyID 116964) have the similar phenomenon in Figure 2a. Another lime outlier near the red cluster is labelled as the spiral (GalaxyID: 110109), but is predicted herein to be the completely round. When inspected, it is really a completely round, i.e. the image numbered 110109 is incorrectly labelled. Figure 2b also shows some outliers like

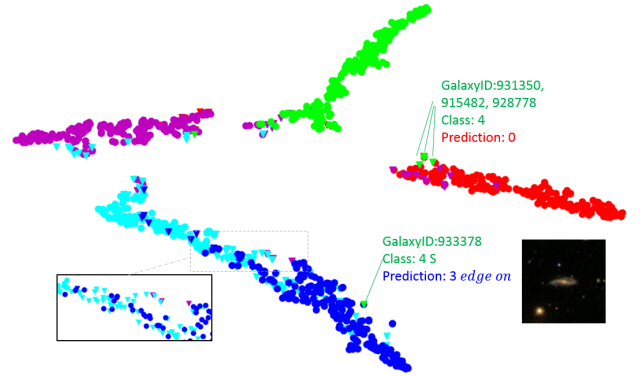
the cigar-shaped (GalaxyID: 981072, 997901) predicted to the in-between, the edge-on (GalaxyID: 924830) predicted to the in-between. After examination, we find the errors are so obvious that even human could recognize them incorrect merely by naked eyes without the aid of any machine.

Figure 3 shows visualizations of activations of the last fully connected layer of CNN 2. Examining the Figure 3a and Figure 3b, we see that the separation between the galaxy classes is almost perfect and each class has a strip distribution. The two dotted ellipses show that 9 in-between are misclassified into the completely round and 16 cigar-shaped are misclassified into the in-between in Figure 3a. This can be understandable that the completely round, the in-between and the cigar-shaped are all smooth galaxy. There is no exact limit to recognize them. We can say that they are misclassified, or they are wrongly labelled and classified correctly as well. The inset in Figure 3b shows many cigar-shaped are misclassified into the edge-on.

Figure 4 shows visualizations of activations of the last average pooling layer of CNN 3. Consider the red points (GalaxyID: 102977, 107539, 122674 and 106544) outlined in Figure 4a, which correspond to the completely round and are predicted to the completely round as well, though

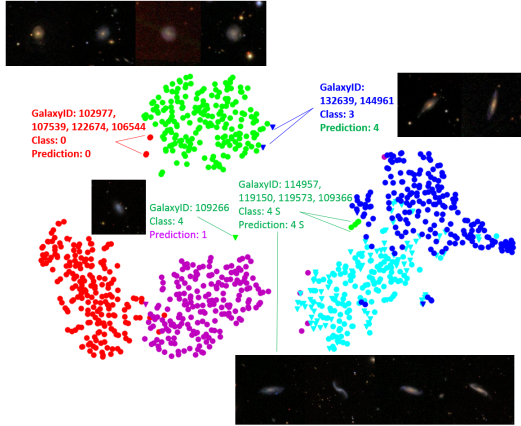


(a) Map of the last fully connected layer of CNN 2 on the training-1000 subset. (Accuracy: 87.1%)

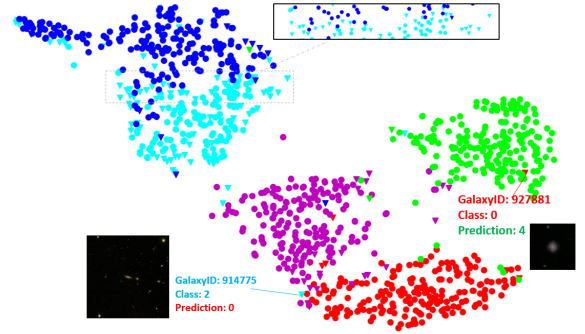


(b) Map of the last fully connected layer of CNN 2 on the testing-1000 subset. (Accuracy: 85.9%)

Figure 3. Visualizations of activations of the last fully connected layer of CNN 2. We color all points by their classes, and mark misclassification by triangle glyphs. Each point is a galaxy image.



(a) Map of the last average pooling layer of CNN 3 on the training-1000 subset. (Accuracy: 91.9%)



(b) Map of the last average pooling layer of CNN 3 on the testing-1000 subset. (Accuracy: 88.0%)

Figure 4. Visualizations of activations of the last average pooling layer of CNN 3. We color all points by their classes, and mark misclassification by triangle glyphs. Each point is a galaxy image.

are placed near the lime cluster corresponding to the spiral. After inspecting, there are three true completely round (GalaxyID: 102977, 107539 and 106544) but preserved the similar structure with the spiral, and one spiral galaxy (GalaxyID: 122674) labelled incorrectly. Another four spiral galaxies (GalaxyID: 114957, 119150, 119573 and 109366) are near the edge-on cluster and the cigar-shaped cluster. When inspected, they are all thin spiral galaxies and look very similar to the edge-on and the cigar-shaped. The outliers in Figure 4b are similar to the outliers in Figure 2b.

There are 2 interesting galaxy images, numbered 109266 and 914775 (GalxyID). 109266 is labelled as the spiral in training-1000 subset, but is mistaken for the in-between both in Figure 2a and Figure 4a. After examining, we find it is a very faint spiral galaxy and very hard to recognize whether it is a spiral or others. 914775 is labelled as the cigar-shaped in testing-1000 subset, but is misclassified into the in-between in CNN 1 shown in Figure 2b and the completely round in CNN 3 shown in Figure 4b, respectively. After inspecting, we find it is too small at the center of the images and really hard

to recognize whether it is the cigar-shaped, the completely round or the in-between, which all belong to smooth galaxy.

The separation among the galaxy classes on training subset is better than on testing subset. It is reasonable because the training subset reaches a higher accuracy and learns a better representations.

Each small cluster like the completely round and the spiral is generally well grouped and almost perfect. And broad clusters like smooth galaxy including the completely round, the in-between and the cigar-shaped tend to be grouped closer together as well, as shown in Figure 3b, Figure 4a and Figure 4b.

The visualizations reveal a fairly surprising phenomenon: the cigar-shaped and the edge-on are intertwined and overlapped, as shown in Figure 2a, Figure 2b, Figure 3a, Figure 3b, Figure 4a and Figure 4b. This implies that the geometry of the cigar-shaped and the edge-on is similar. It is a common sense that the completely round, the in-between and the cigar-shaped are all smooth galaxies and similar, however, the results of visualization indicate that the cigar-

shaped and the edge-on are much closed to together. This finding may help to further optimize the design of GZ2 decision tree.

4 CONCLUSIONS

In this paper we train three CNNs to classify galaxies and learn automatically high-level abstract feature representations, use t-SNE techniques to visualize the high-dimensional feature representations in scatter plots, and explore the underlying structure of the data, and in some cases, the meaning of the data. Our experiments show that visualizations are of help to understand the global structure and the local structure of the galaxy, outliers, clusters with the learned feature representations extracted from CNNs. For example, the same morphological class galaxy images are clustered. A broad class, like smooth galaxy including the completely round, in-between and cigar-shaped, tends to group together and gets closer. It is an interesting phenomenon that the cigar-shaped and edge-on are intertwined. We find a completely round smooth galaxy is incorrectly labelled as spiral galaxy. This proves that the visualizations can help to find outliers in the dataset. It is hoped that this study could contribute to the exploring and understanding of the galaxy image data itself with visualization, then provide valuable feedbacks to galaxy classification system, and facilitate the study of galaxy morphology. Our code is available for download at <https://github.com/Adaydl/GalaxyVisualization>.

In the future we plan to visualize galaxy datasets on more fine-grained classes, e.g., 10 classes that would be more challenging. And we focus on more excellent deep learning algorithms to improve galaxy morphology classification performance and obtain higher quality galaxy feature representations.

ACKNOWLEDGEMENTS

We would like to thank the galaxy challenge, Galaxy Zoo, SDSS and Kaggle platform for kindly sharing data. We acknowledge the financial support from the National Earth System Science Data Sharing Infrastructure (<http://spacescience.geodata.cn>). We are also supported by CAS e-Science Funds (Grand XXH13503-04).

REFERENCES

- Abadi M., et al., 2016, arXiv preprint arXiv:1603.04467
- Aniyan A., Thorat K., 2017, The Astrophysical Journal Supplement Series, 230, 20
- Belkin M., Niyogi P., 2002, in Advances in neural information processing systems. pp 585–591
- Bengio Y., Courville A., Vincent P., 2013, IEEE transactions on pattern analysis and machine intelligence, 35, 1798
- Dieleman S., Willett K. W., Dambre J., 2015, Monthly notices of the royal astronomical society, 450, 1441
- Glorot X., Bengio Y., 2010, in Proceedings of the Thirteenth International Conference on Artificial Intelligence and Statistics. pp 249–256
- Goodfellow I., Bengio Y., Courville A., 2016, Deep learning. MIT press
- Gravet R., et al., 2015, The Astrophysical Journal Supplement Series, 221, 8
- He K., Zhang X., Ren S., Sun J., 2015, in Proceedings of the IEEE international conference on computer vision. pp 1026–1034
- He K., Zhang X., Ren S., Sun J., 2016a, in European Conference on Computer Vision. pp 630–645
- He K., Zhang X., Ren S., Sun J., 2016b, in Proceedings of the IEEE conference on computer vision and pattern recognition. pp 770–778
- Hinton G. E., Roweis S. T., 2003, in Advances in neural information processing systems. pp 857–864
- Hinton G. E., Salakhutdinov R. R., 2006, science, 313, 504
- Hotelling H., 1933, Journal of educational psychology, 24, 417
- Huang G., Liu Z., Weinberger K. Q., van der Maaten L., 2016, arXiv preprint arXiv:1608.06993
- Ioffe S., Szegedy C., 2015, in International Conference on Machine Learning. pp 448–456
- Kim E. J., Brunner R. J., 2016, Monthly Notices of the Royal Astronomical Society, p. stw2672
- Krizhevsky A., Sutskever I., Hinton G. E., 2012, in Advances in neural information processing systems. pp 1097–1105
- LeCun Y., 1998, <http://yann.lecun.com/exdb/mnist/>
- LeCun Y., Bengio Y., Hinton G., 2015, Nature, 521, 436
- Maaten L. v. d., Hinton G., 2008, Journal of Machine Learning Research, 9, 2579
- Nair V., Hinton G. E., 2010, in Proceedings of the 27th international conference on machine learning (ICML-10). pp 807–814
- Netzer Y., Wang T., Coates A., Bissacco A., Wu B., Ng A. Y., 2011, in NIPS workshop on deep learning and unsupervised feature learning. p. 5
- Pedregosa F., et al., 2012, Journal of Machine Learning Research, 12, 2825
- Rauber P. E., Fadel S. G., Falcao A. X., Telea A. C., 2017, IEEE transactions on visualization and computer graphics, 23, 101
- Roweis S. T., Saul L. K., 2000, science, 290, 2323
- Sánchez H. D., Huertas-Company M., Bernardi M., Tuccillo D., Fisher J., 2017, arXiv preprint arXiv:1711.05744
- Simonyan K., Zisserman A., 2014, arXiv preprint arXiv:1409.1556
- Srivastava N., Hinton G. E., Krizhevsky A., Sutskever I., Salakhutdinov R., 2014, Journal of Machine Learning Research, 15, 1929
- Szegedy C., et al., 2015, in Proceedings of the IEEE conference on computer vision and pattern recognition. pp 1–9
- Szegedy C., Vanhoucke V., Ioffe S., Shlens J., Wojna Z., 2016, in Proceedings of the IEEE Conference on Computer Vision and Pattern Recognition. pp 2818–2826
- Szegedy C., Ioffe S., Vanhoucke V., Alemi A. A., 2017, in AAAI. pp 4278–4284
- Tenenbaum J. B., De Silva V., Langford J. C., 2000, science, 290, 2319
- Torgerson W. S., 1952, Psychometrika, 17, 401
- Van Der Maaten L., 2007, Report, 1201, 62
- Van Der Maaten L., 2014, Journal of machine learning research, 15, 3221
- Van Der Maaten L., Postma E., Van den Herik J., 2009, J Mach Learn Res, 10, 66
- Van S. D. W., SchAúnberger J. L., Nuneziglesias J., Boulogne F., Warner J. D., Yager N., Gouillart E., Yu T., 2014, Peerj, 2, e453
- Willett K. W., et al., 2013, Monthly Notices of the Royal Astronomical Society, p. stt1458

This paper has been typeset from a $\text{\TeX}/\text{\LaTeX}$ file prepared by the author.